Dual Liquid Rubber Matrix Based Highly Efficient and Mechanically Robust Layer-by-Layer Organic Solar Cells

Downloaded from: https://research.chalmers.se, 2026-07-14 03:10 UTC

Citation for the original published paper (version of record):
Liao, Y., Xiang, H., Hu, T. et al (2025). Dual Liquid Rubber Matrix Based Highly Efficient and Mechanically Robust Layer-by-Layer Organic
Solar Cells. SUSMAT, 5(2). http://dx.doi.org/10.1002/sus2.70005

N.B. When citing this work, cite the original published paper.

research.chalmers.se offers the possibility of retrieving research publications produced at Chalmers University of Technology. It covers all kind of research output: articles, dissertations, conference papers, reports etc. since 2004. research.chalmers.se is administrated and maintained by Chalmers Library

(article starts on next page)

SusMat

WILEY

SusMat

RESEARCH ARTICLE OPEN ACCESS

Dual Liquid Rubber Matrix Based Highly Efficient and Mechanically Robust Layer-by-Layer Organic Solar Cells

Yuchen Liao[1] | Huimin Xiang[1] | Tianyu Hu[1] | Aziz Saparbaev[2] | Xufan Zheng[1] | Ming Wan[1] | Jingnan Wu[3] | Yating Xie[1] | Shiqi Hu[1] | Qi Xiao[1] | Biao Xiao[1] | Ergang Wang[3] | Xunchang Wang[1] | Renqiang Yang[1]

[1]Key Laboratory of Optoelectronic Chemical Materials and Devices (Ministry of Education), School of Optoelectronic Materials & Technology, Jianghan University, Wuhan, China | [2]Institute of Ion-plasma and Laser Technologies, National University of Uzbekistan, Tashkent, Uzbekistan | [3]Department of Chemistry and Chemical Engineering, Chalmers University of Technology, Göteborg, Sweden

Correspondence: Xunchang Wang (wangxc@jhun.edu.cn) | Renqiang Yang (yangrq@jhun.edu.cn)

Received: 21 September 2024 | **Revised:** 26 November 2024 | **Accepted:** 6 January 2025

Funding: This study was supported by the National Natural Science Foundation of China (52203225, 52073122, 22375077), Key R&D Project of Hubei Province (2022BAA095), Hubei Natural Science Foundation (2022CFB903), the Ministry of Science and Technology of China (2021YFE0113600), the Special Project from Jianghan University (2022XKZX02), and Excellent Discipline Cultivation Project by JHUN (2023XKZ010, 2023XKZ014).

Keywords: cross-linking | flexible organic solar cell | liquid rubber matrix | robust mechanical

ABSTRACT

Developing organic solar cells (OSCs) simultaneously possessing high efficiency and robust mechanical properties is one of crucial tasks to ensure their operational reliability and applicability for emerging wearable devices. However, enhancing their mechanical properties without compromising the electrical properties of high-performance active materials remains a challenge. This work presents a method that overcomes this limitation by embedding a dual liquid rubber (DLR) matrix consisting of tetra-fluorophenyl azide and penta-fluorophenyl end-capped polybutadienes, PFFA and PFF, into layer-by-layer (LBL) films, which enables by a finely controlled film morphology built on strong noncovalent interactions and azide cross-linking chemistry. The resulting LBL film demonstrates a significantly improved stretchability and reduced stiffness of the active layer, with a crack initiation strain that is approximately eight times higher than that of pristine film. The potential of the DLR strategy is demonstrated in PM6:L8-BO flexible solar cells with a power conversion efficiency of 17.7%, which is among the highest efficiencies for flexible OSCs to date. More importantly, the DLR strategy also enables significant bending durability of flexible LBL OSCs that retain 84.2% of their initial performance after 5000 bending cycles. This design concept offers a new strategy for achieving highly efficient and stretchable LBL OSCs.

1 | Introduction

Organic solar cells (OSCs) have attracted considerable attention as a promising energy technology due to their lightweight, solution processing, flexibility, and semitransparency advantages [1–8]. OSCs with high efficiency and mechanical robustness are considered an indispensable prerequisite for ensuring the operational reliability and applicability of future-generation building/vehicle-integrated photovoltaics, self-powered wearable electronics, and portable energy systems [9–12]. Thanks to the significant progress of molecular design, such as BDT-based polymer donors and Y-series small-molecule nonfullerene acceptors, and device engineering, the power conversion efficiencies (PCEs) of OSCs have approached 20% [13–19]. Unfortunately,

Yuchen Liao, Huimin Xiang, and Tianyu Hu contributed equally to this work.

This is an open access article under the terms of the Creative Commons Attribution License, which permits use, distribution and reproduction in any medium, provided the original work is properly cited.

© 2025 The Author(s). *SusMat* published by Sichuan University and John Wiley & Sons Australia, Ltd.

the mechanical properties of these highly efficient OSCs remain far from the requirements on flexible devices, which has been mainly attributed to state-of-art active layers possessing brittle mechanical properties with crack onset strain (COS) values of less than 5% [20–24]. Therefore, there is an urgent need to develop an effective method to enhance the mechanical robustness of OSCs while maintaining high PCE values.

The mechanical properties of active layers strongly depend on the dissipation of strain energy by controlling the molecular backbone conformation and packing motifs [25–28]. From a chemical molecular design perspective, several strategies have been reported to improve the mechanical properties of active layers, such as the incorporation of a flexible conjugation-break spacer in the polymer backbone, the synthesis of molecules that partly embed dynamic bonding in terpolymers, and the construction of single-component active materials containing covalently linked donor and acceptor moieties [29–34]. However, flexible conjugation-break space and dynamic bonding components are typically incorporated as random comonomers, resulting in a randomized distribution of conjugation lengths and specific functional groups, which impact the synthetic batch–batch repeatability of materials. In addition, single-component OSCs have limitations in the form of relatively low PCE values, due to the difficulty of optimizing morphology [35–59]. Another strategy to straightforwardly increase the stretchability of active layers involves the introduction of rubbery insulating polymers, such as PS-b-poly(ethylene-butylene)-b-PS polymers and poly(aryl ether ketone) resins, into binary blends [38–44]. Considering their high ductility but lack of inherent charge transport ability, the selection of material type and the determination of the proportion to incorporate into the blended film serve as critical strategies for improving the stretchability and PCE of OSCs [45–48]. For example, Ye et al. found that PM6:L8-BO blends with 5 wt% PS-b-poly(ethylene-rbutylene)-b-PS polymers achieved simultaneous increases in PCE (15.57%) and COS (9.5%) values compared to blends without the introduction of rubbery insulating polymers (15.42% PCE and 6.9% COS) [50]. Chu et al. showed that the addition of 30% poly(aryl ether ketone) resins into PM6:L8-BO blends afforded a significant enhancement of elongation-at-break from 5.75% to 25.07% while maintaining a superior PCE of the OSCs (15.8%) [44]. Inspired by these studies, establishing a molecular design approach for rubbery insulating polymers that can reinforce the mechanical properties of the active layer without sacrificing electrical performance is worthy of a more in-depth exploration.

Chemical cross-linking serves as a viable approach, generating covalent cross-links in polymer electronic materials, resulting in polymers with higher strain and toughness [49–52]. Unfortunately, few studies have successfully reported high-efficiency cross-linked OSCs because cross-linking agents may deteriorate optoelectronic performance [52]. Other than chemical cross-linking, noncovalent interactions (hydrogen bonds or coordination bonds) are typically introduced to form dynamic networks as energy-dissipating sacrificial linkages and reinforce the mechanical properties of films [53–55]. In addition, the establishment of noncovalent interactions between commonly designed additive and active materials can facilitate the formation of preferable vertical component distributions, enhance molecular crystallinity, and provide better charge transport properties, thus improving the photovoltaic performance [56–58]. Therefore, we suppose that designing insulating polymers with combined multisite cross-links and strong noncovalent bonding could serve as an effective strategy for enabling efficient OSCs with excellent mechanical robustness.

In this work, we synthesized two liquid rubber (LR) matrices consisting of tetra-fluorophenyl azide and penta-fluorophenyl end-capped polybutadienes, PFFA and PFF, which were used as insulating polymers-based additives to realize the improved stretchability and reduced stiffness of the layer-by-layer (LBL) PM6:L8-BO–blended film and simultaneously maintain its high efficiency. The azide-containing end groups of PFFA had the ability to cross-link the alkyl side chains on PM6 through azide/C–H insertion to form a stretchable and elastic PM6-PFFA matrix, which dramatically reinforced the mechanical properties of the composite films [59]. In addition, the presence of strong intermolecular interactions within the composite film due to the utilization of tetra- and penta-fluoro terminal groups in these two LRs possibly provided sufficient dynamic bonds, which could dissipate stress from mechanical deformation, obviating the need to dissipate energy from fracture [60]. In addition, molecular dynamics (MD) simulations and synchrotron x-ray scattering revealed that the tetra-fluorophenyl or per-fluorophenyl end groups could interact with the electropositive main skeleton of PM6 and L8-BO via electrostatic force, and thus reduce the intermolecular interaction energy to allow stronger donor–donor/acceptor–acceptor connections, impeding the disruption of molecular aggregation and resulting in maintained charge transport pathways. With optimal PFFA and PFF content (10 and 20 wt%), the PM6-$PFFA_{10}$:L8-BO-PFF_{20} LBL blends achieved a significant enhancement in elongation-at-break from 6.6% to 48.5% and a reduction in elastic modulus from 265 to 17 MPa while maintaining a superior PCE of the PM6:L8-BO–based LBL flexible OSCs (17.7%). Furthermore, the DLR strategy enabled the significant bending durability of flexible OSCs, which retained their initial performance of 84.2% after 5000 bending cycles at a radius of 4 mm. Therefore, this work established the molecular design concept of guest component LR matrices, which could be used to control the mechanical and electrical properties of blended films, providing a new strategy for the future development of stretchable OSCs.

2 | Results and Discussion

2.1 | Design and Characterization of LRs

The detailed synthetic routes of the two LRs, PFFA and PFF, are shown in Schemes S1 and S2. The reaction between polybutadiene and per-fluorophenyl azide end-capped afforded PFFA, which was fully characterized by ^{1}H, ^{13}C, and ^{19}F-NMR (Figures S1–S6). The utilized flexible backbone structure, polybutadiene, enabled suitable mixing with the active layer without forming large separated domains and resulted in a semiconductor with elastic properties [61]. State-of-art conjugated polymer donor PM6 and nonfullerene acceptor L8-BO were selected as the model to analyze the variations in mechanical properties and photovoltaic performance of OSCs after incorporation of the designed LRs (Figure 1). Obviously, the cross-linking density increases with the augment of PFFA ratio (Table S1). Moreover, the blended

26924552, 2025, 2, Downloaded from https://onlinelibrary.wiley.com/doi/10.1002/sus2.70005 by Chalmers Research - Chalmers University Of Technology , Wiley Online Library on [03/06/2026]. See the Terms and Conditions (https://onlinelibrary.wiley.com/terms-and-conditions) on Wiley Online Library for rules of use; OA articles are governed by the applicable Creative Commons License

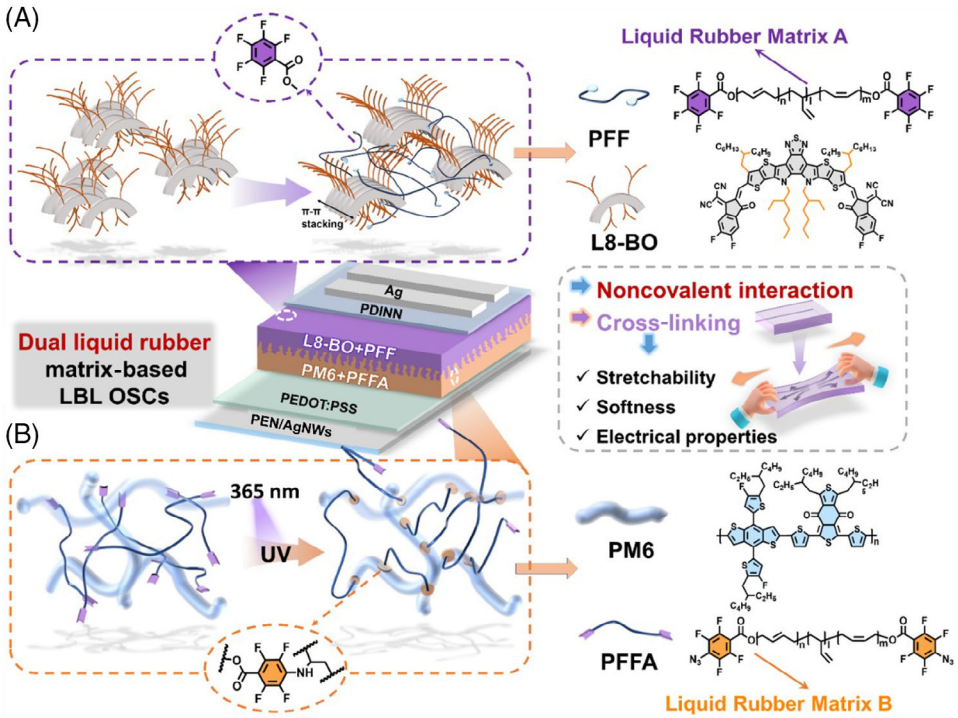

FIGURE 1 | The formation processes of the two liquid rubber matrices of (A) L8-BO-PFF and (B) PM6-PFFA, and corresponding LBL flexible OSCs.

or cross-linked LBL films with PFFA all exhibited uniform mixing (Figure S18). We hypothesize these morphologies may originate from the surface energy compatibility between the two components (conjugated polymer and flexible PFFA backbone). This flexibility can prevent large domain (microscale) phase separation driven by crystallization of the molecules, as has been observed in other systems [62].

We first examined the importance of the cross-linker azide group in photochemical reaction with polymer donor PM6 through Fourier transform infrared (FTIR) spectroscopy analysis of the active layer film before and after ultraviolet–visible (UV–vis) exposure. The chemical peak of 2110 cm^{-1} corresponded to the vibration peak of the azide group of PFFA, which dramatically weakened after exposure to UV light, as shown in Figure S7, indicating the almost complete reaction of the azide group with the PM6 polymer [10]. This was also supported by the UV–vis absorption spectra of the PM6-PFFA film before and after chloroform (CF) rinsing (Figure 2a). As shown in the inset of Figure 2a, when the PM6-PFFA films were not subjected to UV exposure, no polymer was found on the glass substrate after CF washing, with the significantly reduced absorbance of the PM6-PFFA film. By contrast, the film absorption spectrum remained almost unchanged after UV treatment and solvent washing, only exhibiting a slight decrease in the absorbance intensity after rinsing. This indicated that UV treatment was an effective and quick strategy for achieving 3D cross-linking networks within the PM6-PFFA film, and the cross-linking reaction did not damage the conjugated backbone of PM6 and the optoelectronic performance. According to the above observations, we simply elaborated on the cross-linking process and photochemical reaction mechanism of PFFA with the PM6 polymer. When exposed to UV light, the photolysis of the azide groups in PFFA generated highly reactive singlet nitrenes with the emission of nitrogen gas [63]. Then, due to the strong steric hindrance effect, nitrenes were mostly inserted into the C–H bond of the adjacent alkyl chains of the PM6 polymer, instead of reacting with the π conjugated core of the polymer donor, which would disrupt the overall structural conjugation and molecular π–π stacking [64]. Thus, PFFA molecules were bonded onto the alkyl side chains of PM6, resulting in the formation of a 3D cross-linked network that maintained its charge transport pathway (Figure 2b). Besides, when subjected to external strain, the stress within 3D cross-linked network can be transmitted through the dense entanglement to other molecular chains before the chains break. Therefore, the polymer not only consumes the elastic energy of the long chain but also the elastic energy of other entangled chains when a covalent bond breaks, thus achieving high toughness [65].

X-Ray photoelectron spectroscopy (XPS) was subsequently measured for the thin film of pure and composite films to investigate interactions between PFFA and PM6, and between PFF and L8-BO. The XPS spectrum of F1s shows that neat PFFA and PM6 films peak at 687.9 and 687.7 eV (d1s), respectively. In the PM6-PFFA composite film, the peak at 687.7 eV shifts to a higher bond energy (688.0 eV, Figure 2c), indicating that the electron density of F atom decreases. Meanwhile, a similar phenomenon was observed where the F1s XPS spectra of the L8-BO-PFF films exhibited peak shifts to higher bonding energy compared to the pristine L8-BO and PFF films, indicating the formation of conspicuous interactions between the fluorinated end group and photovoltaic materials. Compared to the original PM6 and L8-BO films, the O1s XPS spectra of the PM6-PFFA and L8-BO-PFF films showed obvious peak shifts. As shown in Figure 2c, peaks at 530.9 and 532.1 eV were observed for the original PM6 membrane, and these peaks moved to higher bond energies of 532.0 and 533.3 eV in the PM6-PFFA membrane. The PM6-PFFA film showed a

26924552, 2025, 2, Downloaded from https://onlinelibrary.wiley.com/doi/10.1002/sus2.70005 by Chalmers Research - Chalmers University Of Technology , Wiley Online Library on [03/06/2026]. See the Terms and Conditions (https://onlinelibrary.wiley.com/terms-and-conditions) on Wiley Online Library for rules of use; OA articles are governed by the applicable Creative Commons License

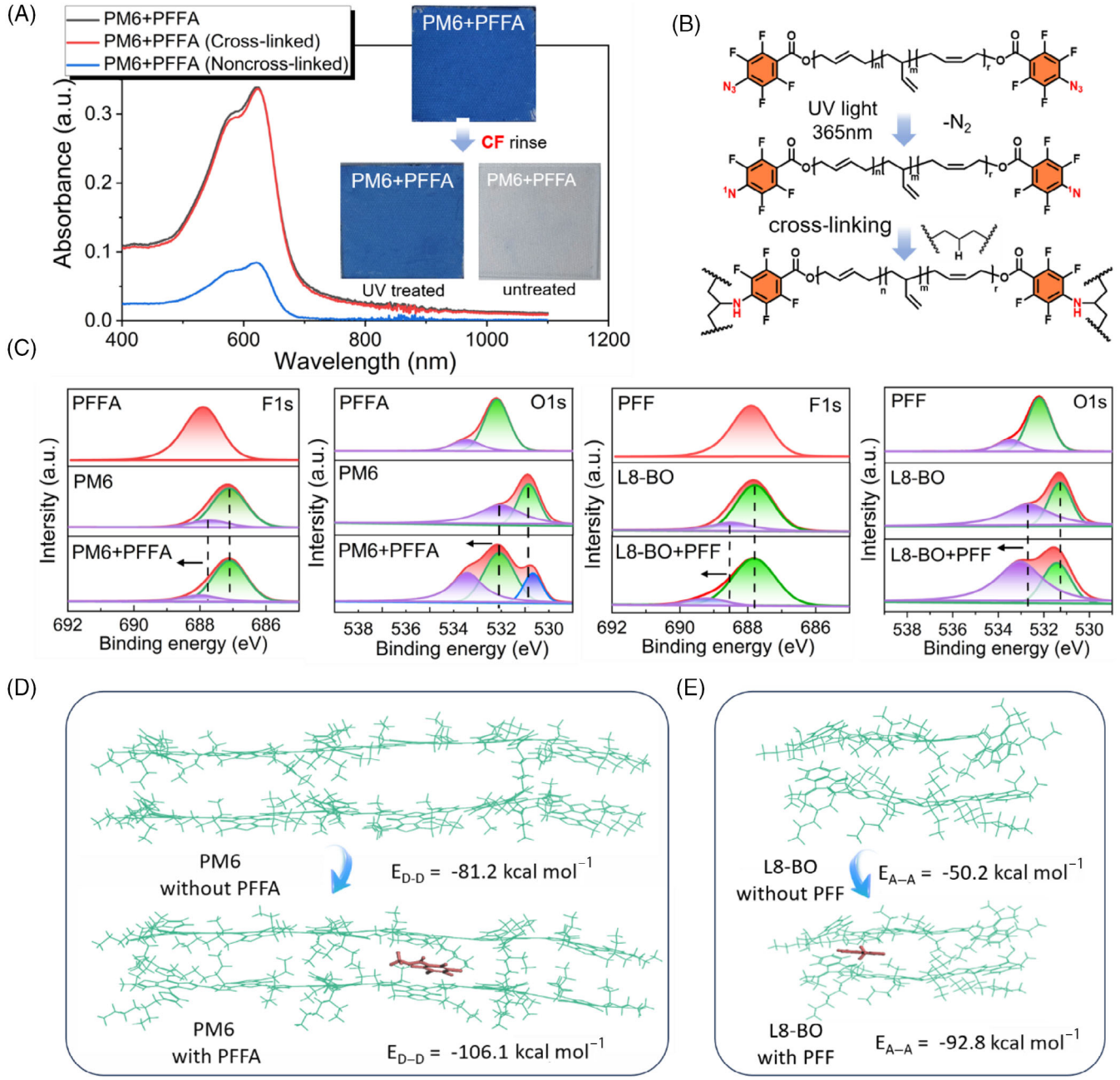

FIGURE 2 | (A) Absorption intensity of PM6 + PFFA with and without UV treatment, (B) the cross-linking process of the PM6-PFFA mechanism, (C) XPS spectra of the pure and composite acceptor and donor films, and intermolecular interactions between (D) D–D and (E) A–A.

new peak at 530.6 eV, indicating interactions between PFFA and PM6. In the L8-BO pure film, peaks at 531.2 and 532.6 eV were observed, which moved to higher bond energies of 531.3 and 533 eV in the L8-BO-PFF film, and the displacement of these peaks indicated a decrease in the electron density of the O atoms of PM6 and L8-BO (Figure 2c) [66]. In these blends, changes in the binding energies of the F1s and O1s peaks indicated noncovalent interactions between the F and O atoms in the PM6-PFFA and L8-BO-PFF films.

These noncovalent interactions were further confirmed by the UV–vis spectra, as illustrated in Figure S8. The 617 nm absorption peak of the PM6 film and the 796 nm absorption peak of the L8-BO film redshifted to 623 and 801 nm after 10 and 20 wt% LR (PFFA and PFF) incorporation, respectively, revealing better molecular packing of both PM6 and L8-BO. Moreover, in addition to the redshift, the obviously enhanced absorption coefficient of PM6-PFFA at 627 nm and L8-BO-PFF at 725 nm, which was improved by ~1.08 times from 9.62×10^4 (neat PM6 film) to 1.04×10^5 cm^{-1} and from 7.02×10^4 (neat L8-BO film) to 7.61×10^4 cm^{-1}. The absorption peak of LBL films also showed the same trend (Figure S9), indicating the additional interactions between PFFA and PM6, and between PFF and L8-BO. Furthermore, according to the DSC results, we found that the pure L8-BO small molecule demonstrated a characteristic melting point (T_m) of 319°C (Figure S10) along with a minor peak at 223°C due to its multidimensional crystalline structure. After incorporating 20 wt% PFF, the melting point of L8-BO shifted from 319°C to 304°C,

26924552, 2025, 2, Downloaded from https://onlinelibrary.wiley.com/doi/10.1002/sus2.70005 by Chalmers Research - Chalmers University Of Technology , Wiley Online Library on [03/06/2026]. See the Terms and Conditions (https://onlinelibrary.wiley.com/terms-and-conditions) on Wiley Online Library for rules of use; OA articles are governed by the applicable Creative Commons License

and the minor peak shifted to 175°C, indicating strong intermolecular interactions between PFF and L8-BO [67, 68]. Therefore, strong intermolecular interactions within the PM6-PFFA and L8-BO-PFF pairs, coupled with the additional formation of a 3D cross-linked network within PM6-PFFA, effectively contributed to exceptional mechanical robustness while maintaining the electronic properties of the semiconductor.

MD simulations were further employed to elucidate how the LRs, PFFA and PFF, interacted with PM6 and L8-BO, affecting their structural order in the solid films. According to snapshots of the simulation results shown in Figure 2d, due to the distinct disparity of the electrostatic potential surface (Figure S11), the end group of PFFA was preferentially located near the main chain of PM6, and PM6 with three repeating D–A units was selected as a structural model to allow another PM6 molecule to adsorb onto. For L8-BO, two simulated moieties (Figure 2e) were constructed, with the PFF moiety adapting parallel, yet center, offset π-stacking. The corresponding interaction energy (E) values between the two PM6 donor molecules and between the two L8-BO molecules were calculated without (i.e., E_{D-D}) and with (i.e., $E_{D-D'}$) the presence of LRs, where the lower the E_{D-D} value, the stronger the intermolecular interactions, and vice versa. Without the assistance of PFFA, the calculated E_{D-D} was around −81.2 kcal mol^{-1}, and this value could become more negative to around −106.5 kcal mol^{-1} with the addition of PFFA, confirming that PFFA could act as a molecular bridge to strengthen the interactions between the adjacent PM6 molecules and form more compact $\pi-\pi$ stacks. The same trend was observed for L8-BO, which showed a reduced interaction energy from −50.2 to −92.7 kcal mol^{-1} (Figure 2e) with the assistance of PFF. Therefore, these results further validated that LRs (PFFA and PFF) could function as a molecular bridge to construct the compact and ordered molecular packing of molecules, thus interconnecting two crystalline domains for the improved orientation alignment of crystallite and elevated charge transport properties.

2.2 | Carrier Mobility and Mechanical Properties of Films With DLR Strategy

The space-charge-limited current (SCLC) method was employed to understand how the incorporation of LRs, PFFA and PFF, affected the carrier mobility of the neat PM6 and L8-BO films. As hypothesized, all neat films treated with LRs (5–30 wt%) demonstrated mobility values of $> 3.8 \times 10^{-4}$ cm^2 V^{-1} s^{-1} (Figure 3a and Tables S2 and S3), comparable to or even greater than films without LRs. Importantly, these neat films treated with LRs exhibited gradually improved stretchability with a COS of > 10% through the film-on-elastomer (FOE) tensile test technique (Figure 3b,c) [69]. Notably, for the L8-BO-PFF composite films, dramatically improved COS values were observed with the addition of a small amount of PFF, which increased more than two-fold higher compared to those without PFF (Figure 3h and Table S6). These results showed that the utilized LR matrices effectively mitigated the trade-off between the carrier mobility and stretchability of the neat films.

We further studied the carrier mobility of the LBL structure rather than the bulk heterojunction film because the inevitable cross-linking reaction would occur after the incorporation of PFFA in the blended films and deteriorate small molecular L8-BO from UV treatment. More importantly, L8-BO-PFFA after UV irradiation was easily washed away from substrate, indicating that PFFA was not cross-linked with L8-BO (Figure S12). The corresponding hole and electron mobility parameters of the PM6-PFFA:L8-BO-PFF LBL films after applying various proportions of LR matrices are shown in Table S4. This DLR strategy (5–20 wt%) did not adversely affect the electrical performance of the LBL film, with all hole and electron mobilities maintained at ~3.0–6.7 $\times 10^{-4}$ cm^2 V^{-1} s^{-1} despite the addition of different PFFA and PFF proportions. Furthermore, because these mobility values were comparable to those observed in PM6:L8-BO LBL or blended films devoid of LR matrices, this suggested that the in situ formation of an elastic polybutadiene derivative–based 3D rubber matrix within the active layer did not interfere with the charge transport pathways. On the contrary, mobility underwent a drastic decline in the PM6-PFFA:L8-BO-PFF LBL films ($< 2.8 \times 10^{-4}$ cm^2 V^{-1} s^{-1}), with a further increase in PFFA and PFF concentrations (> 20 wt%) (Table S4). Since the more balanced carrier mobility could prohibit charge accumulation and recombination, thus contributing to the higher performance of the OSCs, the incorporation of 10 wt% PFFA into PM6 and 20 wt% PFF into L8-BO were selected as the optimal LBL blends.

To further understand how the incorporation of LR matrices, PFFA and PFF, affected the mechanical properties of the LBL blend, the FOE method was used to study the deformation and crack formation of films during slowly stretching condition (Figure 3d and Figure S13). The PM6-PFFA$_{10}$:L8-BO-PFF$_{20}$ films could be stretched up to 25% strain without showing any visible cracks. By contrast, PM6:L8-BO-PFF$_{20}$, PM6-PFFA$_{10}$:L8-BO, and PM6:L8-BO showed dense and micrometer-scale cracks at 15% strain. The modulus values of these four different LBL blends also demonstrated an obviously inverse correlation with stretchability (Figures 3f and S14). Therefore, the PM6-PFFA$_{10}$:L8-BO-PFF$_{20}$ LBL blend could obtain a relatively high COS (39.08 ± 0.60%) and relatively low modulus (1.04 ± 0.06 GPa), indicating that this LBL film with DLR strategy more efficiently dissipated mechanical stresses under strain. In addition, the variations in mechanical parameters were verified by peak force quantitative nanomechanical mapping (PFQNM) derived from AFM, which was required to obtain the force curve. Subsequently, analysis and calculations on the force curve were performed using the DMT model [70]. As shown in Figure 3e and Table S7, the elastic modulus values of PM6:L8-BO, PM6-PFFA$_{10}$:L8-BO, PM6:L8-BO-PFF$_{20}$, and PM6-PFFA$_{10}$:L8-BO-PFF$_{20}$ were 5.11, 3.91, 2.90, and 0.98 GPa, respectively, indicating similar result trends from FOE measurements.

Next, pseudo-free-standing tensile tests were performed by floating the pure film and PM6:L8-BO LBL films on water (FOW), which provided characterization of the intrinsic thin-film mechanics [71]. From the obtained stress–strain curves and compared to the PM6-PFFA$_0$ and L8-BO-PFF$_0$ films, the fracture strains of the PM6-PFFA$_{30}$ and L8-BO-PFF$_{30}$ films increased by 7 times, and the elastic modulus decreased by 15 times. As shown in Figure S15 and Tables S8 and S9, this significant improvement in stretchability and softness originated from the addition of the soft/ductile LR matrix, which had

26924552, 2025, 2, Downloaded from https://onlinelibrary.wiley.com/doi/10.1002/sus2.70005 by Chalmers Research - Chalmers University Of Technology , Wiley Online Library on [03/06/2026]. See the Terms and Conditions (https://onlinelibrary.wiley.com/terms-and-conditions) on Wiley Online Library for rules of use; OA articles are governed by the applicable Creative Commons License

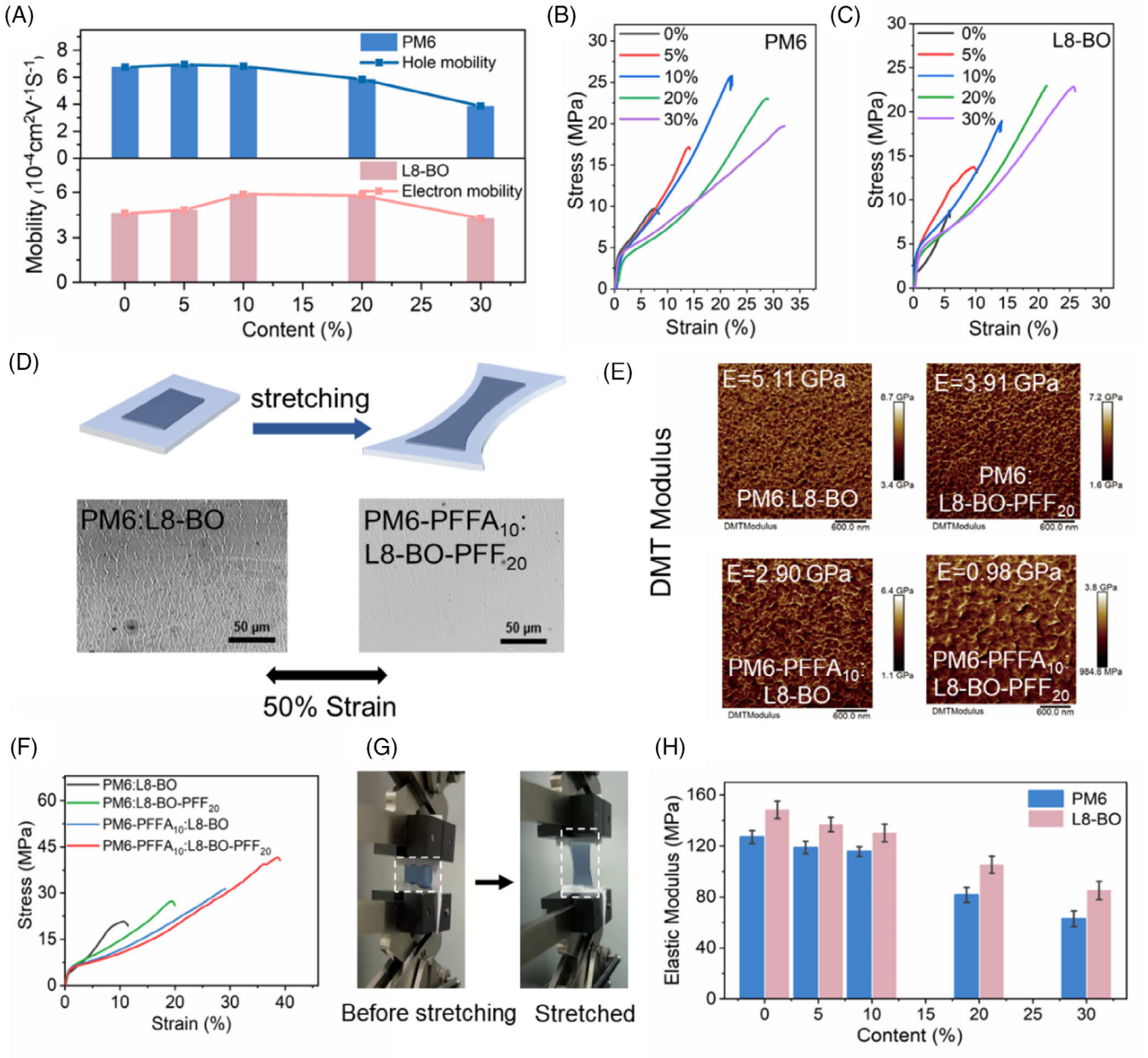

FIGURE 3 | (A) Carrier mobility of neat PM6 and L8-BO, (B) stress–strain curves of the PM6 with different ratios of PFFA by the FOE method, (C) the stress–strain curves of L8-BO with different ratios of PFF by the FOE method, (D) schematic illustration of the stretching of the semiconductor film on a supported TPU substrate and optical microscope images of the PM6:L8-BO film at 50% strain before and after additive addition, (E) DMT modulus images of the PM6:L8-BO films with different PFFA/PFF contents obtained by the PFQNM method, (F) stress–strain (engineering) curves of the PM6:L8-BO layer-by-layer films with varied additive contents measured by FOE, (G) photos of the PM6-PFFA$_{10}$:L8-BO-PFF$_{20}$ film before stretching (left) and stretched to a strain of 100% (right), and (H) elastic modulus of the neat films.

significantly lower elastic modulus values (54 and 71 MPa) and higher fracture strains (30.87% and 19.45%) than pristine PM6 (458 MPa and 4.32%, respectively) and L8-BO (533 MPa and 2.13%, respectively). Similarly, the highest fracture strain of 48.52% was obtained for PM6-PFFA$_{10}$:L8-BO-PFF$_{20}$ among the four LBL films (Figure S16 and Table S10). One reason for the excellent stretchability of the PM6-PFFA$_{10}$:L8-BO-PFF$_{20}$ LBL blend was the synergistic effect of cross-linking and strong intermolecular interactions in the LBL films, which provided many degrees of freedom for the molecular chains to reorient in response to mechanical strain. In addition, the presence of intermolecular interactions from the PM6-PFFA$_{10}$ and L8-BO-PFF$_{20}$ networks possibly provided sacrificial, dynamic bond (i.e., F–π, F–O), which could dissipate stress from mechanical deformation, eliminating the need to dissipate energy from fracture [72]. Thus, the variations in COS and modulus values achieved by the FOW method were consistent with the FOE measurements, which further demonstrated the feasibility of the DLR strategy to improve the stretchability and reduce the stiffness of the blended film.

26924552, 2025, 2, Downloaded from https://onlinelibrary.wiley.com/doi/10.1002/sus2.70005 by Chalmers Research - Chalmers University Of Technology , Wiley Online Library on [03/06/2026]. See the Terms and Conditions (https://onlinelibrary.wiley.com/terms-and-conditions) on Wiley Online Library for rules of use; OA articles are governed by the applicable Creative Commons License

2.3 | Molecular Packing and Phase Structures

Given the significance of morphological behavior in determining device performance and elucidating the enhancement of mechanical properties associated with the DLR strategy in the active layer, we subsequently explored the morphology of these LBL films by AFM tapping mode. As shown in Figure S18, four different types of LBL films displayed nanofibrillar textures with a small square surface roughness (Rq) of around 1.1–1.2 nm before stretching, which was beneficial to the formation of low-resistance ohmic contacts, resulting in higher photocurrents. Of particular interest, the texture of the PM6-$PFFA_{10}$:L8-BO-PFF_{20} film maintained a similar continuous nanofiber morphology, even when subjected to 25% strain, indicating that the semiconductor LR matrix–based film could remain continuous and entangled under mechanical strain. Furthermore, due to the penta-fluorinated end group and azide cross-linking chemistry, the entanglement and interlacing of the composite nanofiber texture possibly provided both stronger interactions and/or attraction to impart better ductility characteristics [73]. By contrast, obvious variations in nano microstructures were observed for the other three LBL films when the strain was applied. Specifically, the original nanofibrils were entirely disordered at 15% strain due to the formation of deep cracks. Therefore, the LBL film obtained using the DLR strategy formed an ideal shape and generated a more efficient charge transfer channel during the stretching and bending processes, which helped to improve the mechanical properties of the film while ensuring the excellent performance of the device. To determine the reason why this DLR strategy could maintain phase separation within the LBL films, we subsequently investigated miscibility between the PM6, L8-BO, and LR matrices through contact angle measurements at room temperature (Figure S19 and Table S11). The relative χ_{aa} of the materials could be calculated from an empirical equation: $\chi_{aa} = K(\sqrt{\gamma_1} - \sqrt{\gamma_2})^2$, where K is a positive constant (typical value of 116×10^3 $m^{-0.5}$), and γ represents the surface tension of the neat films [74]. The resulting low values of $\chi_{PM6/PFFA}$ (0.06) and $\chi_{L8\text{-}BO/PFF}$ (0.03) implied good miscibility between PM6 and PFFA, and between L8-BO and PFF, which could be attributed to the strong molecular interaction of these two pairs. Thus, thermodynamic miscible analysis explained why the original film morphology could be maintained when the DLR strategy was introduced into the LBL films.

To assess the changes in molecular packing and orientation after utilizing the DLR strategy, we first employed grazing-incidence wide-angle x-ray scattering (GIWAXS) measurements on pristine films (PM6 or L8-BO). Figures S20 and S21 display the diffraction images of the GIWAXS measurements and their corresponding linecut profiles for the PM6 and L8-BO–based films under PFFA and PFF treatments, respectively. We observed that the incorporation of these LRs would not damage the preferred face-on molecular orientations of PM6 and L8-BO, due to the (010) π–π stacking and (100) alkyl-to-alkyl stacking signals of these four LBL films located in the out-of-plane (OOP) and in-plane (IP) directions, respectively. In addition, for both PM6 and L8-BO, the relative degree of crystallinity (rDOC) and coherence lengths (CLs) of the (010) diffractions of films with LR treatment (< 30% w/w) were slightly larger than the corresponding pristine films (Figure S22 and Table S12). This facilitated vertical charge transport within the films, which was favorable for realizing promising J_{sc} and FF values in OSCs.

As shown in Figure 4a,b, the GIWAXS images of the LBL films revealed that the preferential face-on orientation could also be maintained using the DLR strategy. Interestingly, among the four different LBL films, the PM6-$PFFA_{10}$:L8-BO-PFF_{20} films exhibited the most compact π–π stacking distances of 3.58 Å (Table S13), with the highest rDOC values as determined from the (010) diffraction peak intensity. These observed nanoscale morphology variations of PM6-$PFFA_{10}$:L8-BO-PFF_{20} obtained using the DLR strategy were consistent with the high carrier mobilities data, which was beneficial for effective exciton dissociation and favorable charge transport in devices. These results confirmed our hypothesis, indicating that embedding end group–modified LR matrices, such as PFF and PFFA, resulted in the construction of strong F–F and F–O noncovalent interactions and molecular cross-links within the active layers, which was beneficial for realizing strong molecular stacking without sacrificing electrical properties.

The microstructure evolution process under stretching served as the basis for exploring the mechanical durability of active layers. Thus, LBL films under stretching were first analyzed to understand the microstructural evolution mechanism. The 2D patterns, diffraction intensity, and CL values of PM6:L8-BO under various strains were described, as shown in Figure 4c, and the crystallographic information and its variation tendency were summarized, as shown in Tables S14 and S15. No obvious changes in the 2D patterns of the active films were observed, while the intensities of both (100) and (010) decreased in all directions with an increase in strain. The change in d-spacing of (100) and (010) originated from the variations in molecular packing distance in the PM6 and L8-BO crystallites. The reduced CL of (100) and (010) and attenuated lamellar packing were possibly attributed to the crystallite rotation and crystallographic deformation of PM6 and L8-BO. The microstructural variations of the PM6-$PFFA_{10}$:L8-BO-PFF_{20}–blended films under various strains are displayed in Figure 4e. Unlike pristine binary blends, the characteristic peaks distinctly changed in the 2D patterns. The (010) intensity dramatically decreased along the equatorial direction and slightly increased along the meridian direction, while the (100) intensity demonstrated an opposite tendency. As shown in Figure 4d,f, the PM6:L8-BO blend showed rapid crystallite minish and puny orientation under small strain, indicating the structural brittleness of the PM6:L8-BO–blended films. The PM6-$PFFA_{10}$:L8-BO-PFF_{20}–blended films showed slow crystallite reduction and obvious crystallite orientation compared to the PM6:L8-BO blend, indicating improved structural stability, which was possibly due to the dynamic bonds dissipating the stress from mechanical deformation, making it immune to crystallite breakage and slippage [75].

According to the above results, we schematically analyzed the mechanism of stretchable PM6-$PFFA_{10}$:L8-BO-PFF_{20}. As shown in Figure 4g, the significant increase in stretchability by adding PFFA and PFF was primarily due to three points. First, the formation of elastic networks of PM6-PFFA and L8-BO-PFF increased chain interactions and tie chains. The noncovalent cross-linking sites (F–O, F–π) within the elastic networks could provide an

26924552, 2025, 2, Downloaded from https://onlinelibrary.wiley.com/doi/10.1002/sus2.70005 by Chalmers Research - Chalmers University Of Technology , Wiley Online Library on [03/06/2026]. See the Terms and Conditions (https://onlinelibrary.wiley.com/terms-and-conditions) on Wiley Online Library for rules of use; OA articles are governed by the applicable Creative Commons License

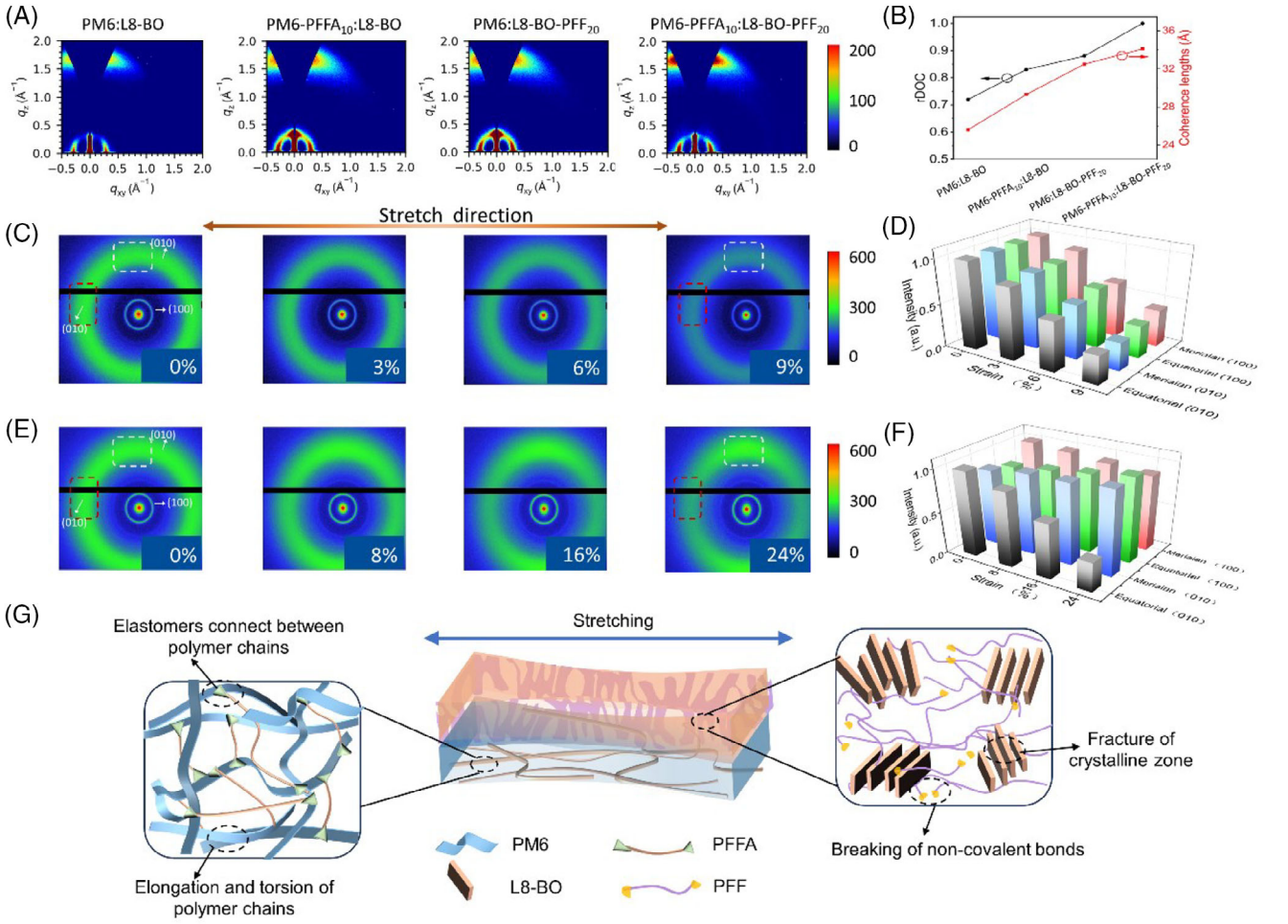

FIGURE 4 | (A and B) GIWAXS patterns of the LBL layers without and with LR treatment and the corresponding rDOC calculated from (010) diffraction, representative 2D patterns from the WAXS transmission model for (C) PM6:L8-BO films and (E) PM6-PFFA$_{10}$:L8-BO-PFF$_{20}$ films under various strains, (D–F) corresponding crystallographic intensity and its orientation variation tendency, and (G) schematic diagram of the morphology changes of PFF and PFFA during the stretching process of the LBL layers using the DLR strategy.

additional strain energy dissipation mechanism through the breakage of these reversible bonds. Another important factor was that PFFA and PFF could act as molecular bridges to interconnect two crystalline domains and construct an integrated elastic rubber, simultaneously improving charge transport properties and mechanical durability.

2.4 | Photovoltaic Properties of the LBL OSCs Using DLR Strategy

The current density–voltage (J–V) characteristic curves under AM 1.5G illumination for the best-performing devices were plotted, as shown in Figure 5a, and the detailed device parameters are summarized in Table 1. The PM6-PFFA$_{10}$:L8-BO and PM6:L8-BO-PFF$_{20}$–based OSCs demonstrated comparative performance as the controlled PM6:L8-BO (17.7%)–based OSCs, with PCEs of 18.2% and 18.7%, respectively. However, the PCE was found to increase in the PM6-PFFA$_{10}$:L8-BO-PFF$_{20}$–based OSCs (19.2%), and the main parameters that contributed to the increase in PCE were J_{sc} and FF. Specifically, the J_{sc} and FF values of the PM6:L8-BO blend slightly increased to J_{sc} = 26.6 mA cm^{-2} and FF = 80.3% for the PM6-PFFA$_{10}$:L8-BO-PFF$_{20}$ blend. The reason for the obviously improved J_{sc} value in the PM6-PFFA$_{10}$:L8-BO-PFF$_{20}$ OSCs could be attributed to the enhanced dielectric properties and built-in-potential of the LBL layer [76]. In addition, the excellent FF of the PM6-PFFA$_{10}$:L8-BO-PFF$_2$ blend indicated that blending with LR matrices, with cross-linking reactions and strong intermolecular interaction effects, would not disrupt the exciton dissociation and charge transport pathways. As shown in Figure 5b, integrated J_{sc} from the external quantum efficiency (EQE) curves was consistent with the J–V measurements. Thus, the DLR strategy possibly did not induce additional trap defects in the LBL layers, and the charges could pass freely, as discussed below.

SCLC measurements via hole-only devices were used to evaluate the trap density (n_{trap}) values of the devices (Figure S23). The n_{trap} values were determined from the trap-filled voltage (V_{TFL}) evaluated using the following equation:

$$V_{TFL} = en_{trap}L^2/(2\varepsilon\varepsilon_0),$$

where L is the thickness of the LBL film, ε denotes the relative dielectric constant, and ε_0 is the vacuum permittivity [77]. Among all tested devices, the PM6-PFFA$_{10}$:L8-BO-PFF$_{20}$ devices

26924552, 2025, 2, Downloaded from https://onlinelibrary.wiley.com/doi/10.1002/sus2.70005 by Chalmers Research - Chalmers University Of Technology , Wiley Online Library on [03/06/2026]. See the Terms and Conditions (https://onlinelibrary.wiley.com/terms-and-conditions) on Wiley Online Library for rules of use; OA articles are governed by the applicable Creative Commons License

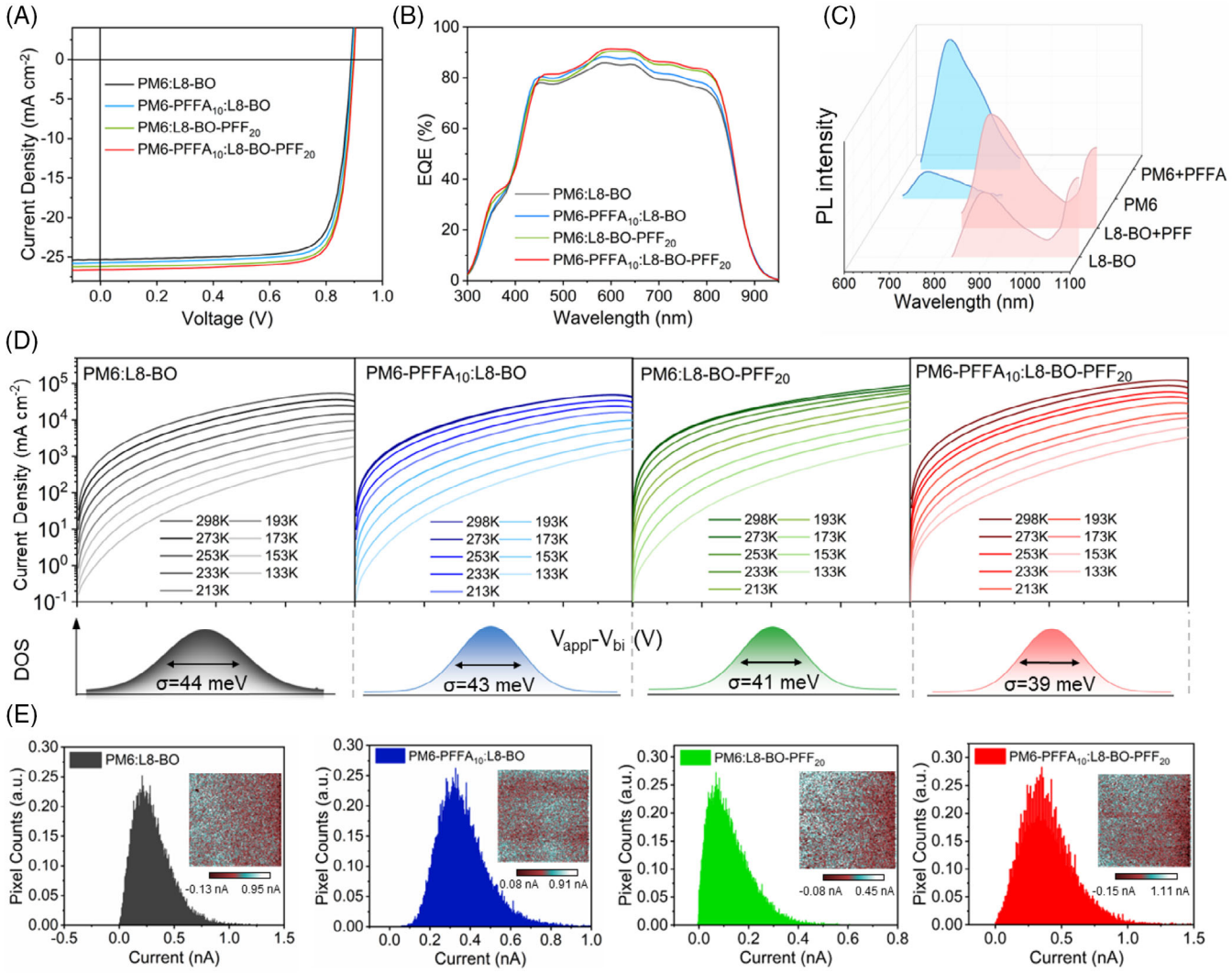

FIGURE 5 | (A) *J–V* curves of rigid OSCs with a conventional structure of ITO/PEDOT:PSS/active layer/PNINN/Ag in this work; (B) EQE curves of rigid OSCs with various types of LBL layers; (C) PL curves of the PM6, PM6 + PFFA, L8-BO, and L8-BO + PFF films; (D) temperature-dependent SCLC curves of the OSCs with various types of LBL layers and corresponding energy disorder values; and (E) AFM current distribution and conductive AFM images of the four types of thin films.

TABLE 1 | Optimized photovoltaic characteristics achieved by rigid and flexible OSCs without and with LR treatment based on the illumination of AM 1.5G, 100 mW cm^{-2}.

Device	J_{sc} (mA cm^{-2})	J_{sc}[a] (mA cm^{-2})	V_{oc} (V)	FF (%)	PCE[b] (%)
PM6:L8-BO[a] (rigid)	25.3	24.7	0.889	78.6	17.7 (17.3 ± 0.4)
PM6-$PFFA_{10}$:L8-BO[a] (rigid)	25.7	24.9	0.891	79.4	18.2 (17.7 ± 0.5)
PM6:L8-BO-PFF_{20}[a] (rigid)	26.2	25.5	0.897	79.8	18.7 (18.5 ± 0.3)
PM6-$PFFA_{10}$:L8-BO-PFF_{20}[a] (rigid)	26.6	25.8	0.898	80.3	19.2 (18.9 ± 0.3)
PM6:L8-BO[b] (flexible)	24.9	24.4	0.854	75.6	16.1 (15.7 ± 0.4)
PM6-$PFFA_{10}$:L8-BO[b] (flexible)	25.3	24.6	0.860	76.3	16.6 (16.0 ± 0.5)
PM6:L8-BO-PFF_{20}[b] (flexible)	25.7	24.6	0.864	77.0	17.1 (16.7 ± 0.4)
PM6-$PFFA_{10}$:L8-BO-PFF_{20}[b] (flexible)	26.2	25.2	0.868	77.8	17.7 (17.2 ± 0.5)

[a]Calculated from the EQE curve.

[b]The values in parentheses are the average values with standard deviation obtained from 15 devices.

26924552, 2025, 2, Downloaded from https://onlinelibrary.wiley.com/doi/10.1002/sus2.70005 by Chalmers Research - Chalmers University Of Technology , Wiley Online Library on [03/06/2026]. See the Terms and Conditions (https://onlinelibrary.wiley.com/terms-and-conditions) on Wiley Online Library for rules of use; OA articles are governed by the applicable Creative Commons License

demonstrated the lowest n_{trap} values (hole-n_{trap} values of 3.64×10^{15}), which was consistent with the OSC performance results provided in Table 1 and could be attributed to the ordered molecular packing of the PM6-PFFA$_{10}$:L8-BO-PFF$_{20}$ films. Second, photoluminescence (PL) measurements were used to investigate the effect of the dual-insulating polymer strategy on photoinduced charge transfer in the LBL layer [78]. As shown in Figure 5c, the PM6-PFFA$_{10}$ and L8-BO-PFF$_{20}$ films exhibited higher PL intensity than neat PM6 and L8-BO, suggesting that the incorporation of the LR matrix led to carrier accumulation at the interface of the blended film without forming traps. We further investigated the effect of the DLR strategy on energetic disorder inside the devices via temperature-dependent hole transport measurements [79], as expressed in the following formula:

$$\mu_0 = \mu_\infty \exp\left[-\left(\frac{2\sigma}{3kT}\right)^2\right],$$

where k is the Boltzmann constant, T denotes temperature (Kelvin), and μ_∞ represents the mobility at an infinite temperature. The plots of the hole zero-field mobilities of the four different types of LBL devices, as a function of $1/T^2$, and the corresponding fitted straight curves are shown in Figures 5d and S24. The calculated σ values for the PM6:L8-BO–, PM6-PFFA$_{10}$:L8-BO–, PM6:L8-BO-PFF$_{20}$–, and PM6-PFFA$_{10}$:L8-BO-PFF20–based devices were 44, 43, 41, and 39 meV, respectively. These results indicated that the DLR strategy could decrease the number of trapped density of states in the LBL films, and the electrons exhibited reduced probability for trapping at tailed states and combined with the holes. Furthermore, charge recombination behavior inside the OSCs was analyzed from the dependence of J_{sc} on incident light intensity (P_{light}) [80]. A power-law function correlation was provided by $J_{sc} \propto P_{light}{}^{S}$, in which $S = 1$ indicated that the bimolecular recombination process of free carriers was negligible. As shown in Figure S25, similar S values were observed in these four LBL devices, with the PM6-PFFA$_{10}$:L8-BO-PFF$_{20}$–based devices showing the slightly largest values of 0.85, thereby revealing that few bimolecular recombination losses occurred in the device with the DLR strategy and also reflected the high J_{sc} value in this device. The photogenerated current density (J_{ph}) versus the effective voltage (V_{eff}) was also investigated (Figure S26) [81], and the exciton dissociation probability $P(E,T)$ values were 0.978, 0.982, 0.983, and 0.998 for the PM6:L8-BO–, PM6-PFFA$_{10}$:L8-BO–, PM6:L8-BO-PFF$_{20}$–, and PM6-PFFA$_{10}$:L8-BO-PFF$_{20}$–based devices, respectively. This further confirmed that efficient exciton dissociation occurred at interfaces employing the DLR strategy. We also used conductive AFM to directly locate the photocurrent changes in these LBL films [82]. As shown in Figure 5e, similar averaged currents around 0.3–0.6 nA were obtained for these four films, indicating that the use of the DLR strategy had almost no negative effects on the photocurrent generation of the blended films. Following the above analysis, we found that the introduction of LR matrices, PFFA and PFF, in the PM6:L8-BO LBL films did not induce additional deep-level charge-trapping states and had a less negative effect on exciton dissociation and transport. Thus, the advantage of the DLR strategy was realized, which could reinforce the mechanical properties of the active layer without sacrificing electrical performance.

We subsequently fabricated flexible devices with a PEN/AgNW/PEDOT:PSS/LBL active layer/PDINN/Ag architecture. The related device parameters are given in Table 1, with the plotted J–V curves shown in Figure 6a. The PM6-PFFA$_{10}$:L8-BO-PFF$_{20}$ film displayed a high PCE of 17.7%, with a V_{oc} of 0.868 V, a J_{sc} 26.2 mA cm^{-2}, and an FF of 77.8% in the flexible device, exceeding that of the PM6:L8-BO (16.1%)–, PM6-PFFA$_{10}$:L8-BO (16.6%)–, and PM6:L8-BO-PFF$_{20}$ (17.1%)–based flexible devices. To the best of our knowledge, the PCE of 17.7% was achieved in this work, which represented one of the highest PCE values among all types of flexible OSCs reported to date (Figure S29 and Table S16). To ensure comprehensiveness, the EQE spectra of these devices were also obtained, as shown in Figure 6b. We then fabricated 50 flexible OSCs utilizing the PM6-PFFA$_{10}$:L8-BO-PFF$_{20}$ LBL system, which exhibited an average PCE of $17.2 \pm 0.5\%$ (Figure 6c). The relatively narrow PCE distribution suggested good reproducibility in the fabrication of flexible LBL OSCs employing the DLR strategy.

We further carried out bending durability tests for flexible LBL OSCs with and without the DLR strategy. Figure S27 shows a schematic diagram of the stress on the flexible device during the bending process, and the bending strain of the flexible device is estimated to be ≈0.8% by simulating the bending process of FOSCs at a bending radius of 4 mm. The detailed calculation process of bending strain is discussed in Supporting Information. The flexible OSCs with PM6-PFFA$_{10}$:L8-BO-PFF$_{20}$ retained 84.2% of their initial PCE after 5000 bending cycles with a bending radius of 4 mm (Figure 6d) [83]. By contrast, the OSCs using bare PM6:L8-BO maintained only 31.0% of their initial PCE after 3000 bending cycles. The improved bending durability enabled by the DLR strategy could be explained by the following possible reasons. First, the incorporation of the LR matrices within the LBL layers provided a soft medium, which increased the toughness at the brittle LBL active layer and the interface between the donor and acceptor, thus enhancing mechanical reliability. Second, the formed cross-linking networks via the azide chemistry reaction and the presence of intermolecular interactions due to the utilization of tetra- and penta-fluoro terminal groups provided sufficient covalent and dynamic bonds, which could dissipate the stress from mechanical deformation, obviating the need to dissipate energy from fracture, as evidenced by the absence of obvious crack formation after blending the PM6:L8-BO films and spin coating on TPU (Figure S13). Avoiding this photoactive fracture was beneficial for controlling disruption in photocarrier transport and enhancing the photovoltaic performance of flexible OSCs. In addition, the electronegative fluorinated end groups were adsorbed on the electropositive backbone of the donor and acceptor, which increased E_{D-D} and E_{A-A}, leading to enhanced structural order with shortened π–π stacking distance and maintained charge transport ability. The use of PFF and PFFA provided the original excellent morphology without inducing elevated trap density, with no negative effect on exciton dissociation and charge transport in LBL OSCs.

Finally, we tracked the PCE evolution with and without using the DLR strategy to assess the long-term operating stability of flexible OSCs (Figure 6e). The maximum power point output was continuously analyzed under constant full simulated AM 1.5G solar illumination (multicolor LED-based simulator with power equivalent to 100 mW cm^{-2}). The control PM6:L8-BO device

26924552, 2025, 2, Downloaded from https://onlinelibrary.wiley.com/doi/10.1002/sus2.70005 by Chalmers Research - Chalmers University Of Technology , Wiley Online Library on [03/06/2026]. See the Terms and Conditions (https://onlinelibrary.wiley.com/terms-and-conditions) on Wiley Online Library for rules of use; OA articles are governed by the applicable Creative Commons License

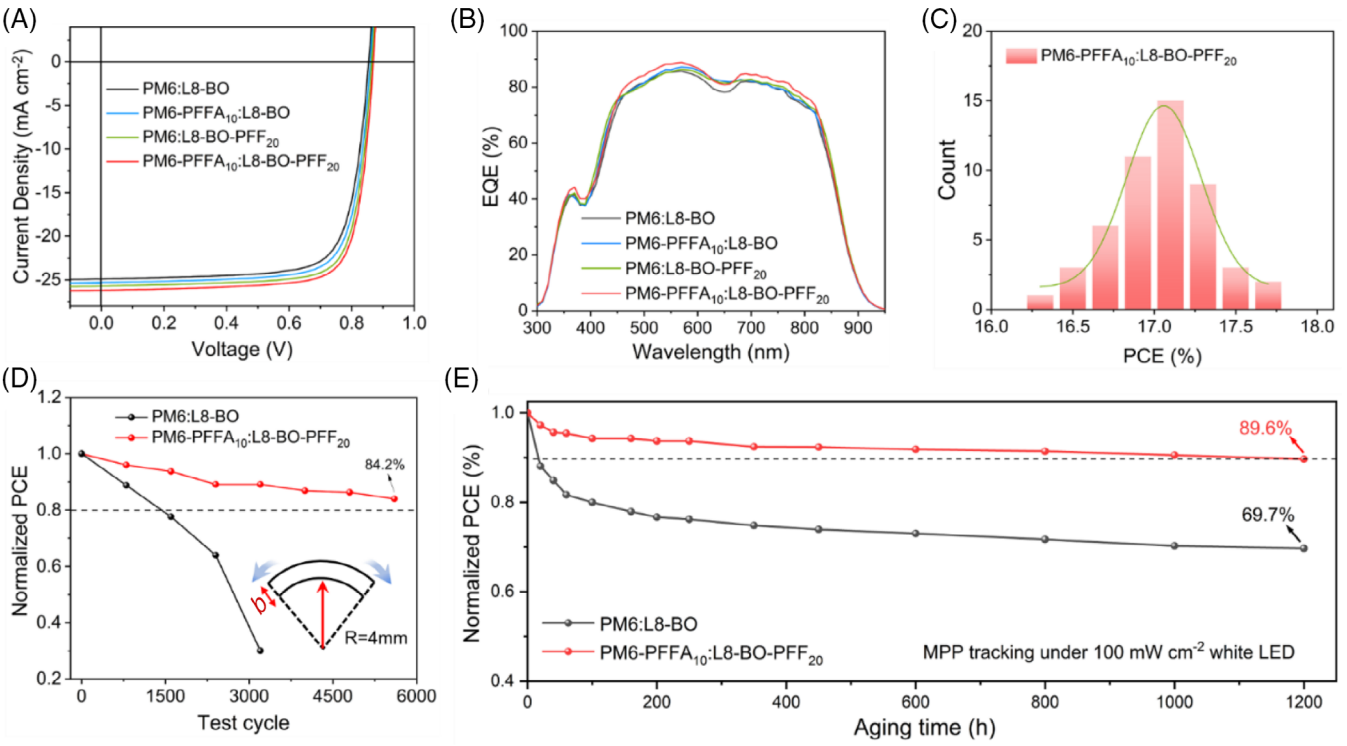

FIGURE 6 | (A) *J–V* curves of the four flexible OSCs based on PM6:L8-BO with and without LR matrices treatment, (B) corresponding EQE curves, (C) PCE distribution histogram of 50 individual target OSCs using the DLR strategy, (D) normalized PCE change of flexible devices with and without the DLR strategy after consecutive bending cycles with a radius of 4 mm, and (E) operational stability of the OSCs with and without the DLR strategy at the MPP in N_2 under white LED illumination with an equivalent effective irradiance of one sun.

suffered a severe drop of 40% in its initial PCE value after aging for 1200 h, while the T_{80} lifetime (80% degradation of initial value) evaluated from the corresponding curves was as low as 110 h. In contrast, the device with DLR demonstrated notably enhanced stability under the same operational conditions, maintaining 89.6% of its initial PCE after 1200 h of continuous operation. Molecular migration and morphology disruption were significantly suppressed by incorporating proper LR matrices in the LBL layer after long-term operation, as evidenced by the AFM measurements (Figure S28). These encouraging results demonstrated the significant potential of using the DLR strategy for improving LBL OSCs for high efficiency, stretchability, and stability.

3 | Conclusions

In summary, we successfully demonstrated that dual-embedded LRs consisting of tetra-fluorophenyl azide and penta-fluorophenyl end-capped polybutadienes, PFFA and PFF, provided a simple and effective strategy for enhancing stretchability and maintaining the electronic properties of high-efficiency LBL OSCs. The core idea involved the finely controlled composite film morphology built on azide chemistry, which took advantage of its cross-linking reactivities with azide/C–H insertion to form a stretchable and elastic matrix. The resulting covalent bonds between the PPFA and semiconductor materials could dramatically reinforce the mechanical properties of the active layers. The presence of strong intermolecular interactions due to the utilization of tetra- and penta-fluoro terminal groups possibly provided sufficient dynamic bonds that could dissipate the stress from mechanical deformation, obviating the need for dissipating energy from fracture. In addition, the electronegative fluorinated end groups adsorbed on the electropositive backbone of the donor and acceptor, which increased E_{D-D} and E_{A-A}. This led to enhanced structural order with a shortened π–π stacking distance and maintained charge transport ability. With optimal PPF and PFFA content (10 and 20 wt%), the LBL film achieved a significant enhancement in elongation-at-break from 6.6% to 48.5% and reduction in elastic modulus from 265 to 17 MPa while maintaining the superior PCE of the PM6:L8-BO–based flexible OSCs (17.7%). The DLR strategy also enabled the significant bending durability of flexible LBL OSCs, which retained their 84.2% initial performance after 5000 bending cycles at a radius of 4 mm. This proposed strategy for constructing multifunctional DLR may play an important role in promoting the flexibility of highly efficient LBL OSCs and the development of practical wearable electronics.

4 | Experimental

4.1 | Solar Cell Device Fabrication

The rigid device structure used in this work is ITO/PEDOT:PSS/active layer/PDINN/Ag. The ITO-coated glass substrates were sonicated successively with detergent, deionized water, acetone, and isopropanol and dried with nitrogen flow. Immediately prior to device fabrication, the substrates were cleaned by oxygen plasma for 25 min. And then,

26924552, 2025, 2, Downloaded from https://onlinelibrary.wiley.com/doi/10.1002/sus2.70005 by Chalmers Research - Chalmers University Of Technology , Wiley Online Library on [03/06/2026]. See the Terms and Conditions (https://onlinelibrary.wiley.com/terms-and-conditions) on Wiley Online Library for rules of use; OA articles are governed by the applicable Creative Commons License

the PEDOT:PSS was spin-coated onto the ITO substrate and treated with thermal annealing for 15 min at 150°C. Then, the substrates were transferred to the N_2-filled glovebox. For the LBL device, PM6 was dissolved in chlorobenzene (CB) solvent at a concentration of 10 mg mL^{-1}, while L8-BO was dissolved in the CF solvent at a concentration of 10 mg mL^{-1}. A total of 10 wt% PFFA was added to the donor to obtain PM6-$PFFA_{10}$ solution, and 20 wt% PFF was added to the recipient solution to obtain L8-BO-PFF_{20} solution. After adding 0.25% v/v CN in L8-BO-PFF solution, and blend solutions were stirred for 20 min. Then the PM6 or PM6-$PFFA_{10}$ solution was spin-coated on the PEDOT:PSS-coated substrates, and the L8-BO or L8-BO-PFF_{20} solution was deposited. The obtained four different LBL active layers were treated with thermal annealing at 85°C for 5 min. Then, the PDINN solution (in CH_3OH) was spin-coated as electron transport layer. Finally, Argentum (100 nm) was evaporated onto the active layer stack at a vacuum of $\sim 2\times10^{-4}$ Pa to form the top electrode. The effective area of the device is 0.042 cm^2. The current density–voltage (*J–V*) characteristics were measured with a Keithley 2450 source measurement unit. The OSCs were measured under an irradiation intensity of 100 mW cm^{-2} (AM 1.5G) by a Newport solar simulator.

The flexible photovoltaic cells were fabricated with the conventional structure (PEN/AgNWs/PEDOT:PSS/active layers/PDINN/Ag). The PEDOT:PSS layers were treated at 100°C for 20 min. Other processes are consistent with those of devices based on the glass substrates.

Acknowledgments

The authors are deeply grateful to the National Natural Science Foundation of China (52203225, 52073122, 22375077), Key R&D Project of Hubei Province (2022BAA095), Hubei Natural Science Foundation (2022CFB903), the Ministry of Science and Technology of China (2021YFE0113600), the Special Project from Jianghan University (2022XKZX02), and Excellent Discipline Cultivation Project by JHUN (2023XKZ010, 2023XKZ014) and cooperation to Arifov Institute of Ion-Plasma and Laser Technologies of Uzbekistan Academy of Sciences.

Conflicts of Interest

The authors declare no conflicts of interest.

References

1. J. S. Park, G. U. Kim, S. Lee, et al., "Material Design and Device Fabrication Strategies for Stretchable Organic Solar Cells," *Advanced Materials* 34, no. 31 (2022): 2201623.

2. J. Yao, Q. Chen, C. Zhang, Z. Zhang, and Y. Li, "Perylene-Diimide-Based Cathode Interlayer Materials for High Performance Organic Solar Cells," *SusMat* 2, no. 3 (2022): 243–263.

3. S. Chu and A. Majumdar, "Opportunities and Challenges for a Sustainable Energy Future," *Nature* 488, no. 7411 (2012): 294–303.

4. Q. He, P. Ufimkin, F. Aniés, et al., "Molecular Engineering of Y-Series Acceptors for Nonfullerene Organic Solar Cells," *SusMat* 2, no. 5 (2022): 591–606.

5. T. Kim, J.-H. Kim, T. E. Kang, et al., "Flexible, Highly Efficient All-Polymer Solar Cells," *Nature Communications* 6, no. 1 (2015): 8547.

6. D. Zhang, Y. Wu, C. Yan, et al., "Simultaneously Improving Stretchability and Efficiency of Flexible Organic Solar Cells by Incorporating a Copolymer Interlayer in Active Layer," *Advanced Functional Materials* 8, no. 46 (2024): 2407681.

7. Z. Chen, J. Zhu, D. Yang, et al., "Isomerization Strategy on a Non-Fullerene Guest Acceptor for Stable Organic Solar Cells With Over 19% Efficiency," *Energy & Environmental Science* 16, no. 7 (2023): 3119–3127.

8. Q. Zhu, J. Xue, H. Zhao, et al., "Highly Efficient Organic Solar Cells With Superior Deformability Enabled by Diluting the Small Molecule Acceptor Content," *Journal of Materials Chemistry A* 10, no. 15 (2022): 8293–8302.

9. D. J. Lipomi, B. C. K. Tee, M. Vosgueritchian, and Z. Bao, "Stretchable Organic Solar Cells," *Advanced Materials* 15, no. 15 (2011): 1771–1775.

10. Z. Wang, D. Zhang, M. Xu, et al., "Intrinsically Stretchable Organic Solar Cells With Simultaneously Improved Mechanical Robustness and Morphological Stability Enabled by a Universal Crosslinking Strategy," *Small* 18, no. 26 (2022): 2201589.

11. J. Qiu, Q. Zhou, M. Yu, et al., "Modulating CsPbI," *SusMat* 3, no. 6 (2023): 894–908.

12. A. X. Chen, A. T. Kleinschmidt, K. Choudhary, and D. J. Lipomi, "Beyond Stretchability:Strength, Toughness, and Elastic Range in Semiconducting Polymers," *Chemistry of Materials* 32, no. 18 (2020): 7582–7601.

13. J. W. Lee, H. G. Lee, E. S. Oh, et al., "Rigid- and Soft-Block-Copolymerized Conjugated Polymers Enable High-Performance Intrinsically Stretchable Organic Solar Cells," *Joule* 8, no. 1 (2024): 204–223.

14. L. Tian, C. Liu, and F. Huang, "Recent Progress in Side Chain Engineering of Y-Series Non-Fullerene Molecule and Polymer Acceptors," *Science China Chemistry* 67, no. 3 (2024): 788–805.

15. Q. Fan, Q. Xiao, H. Zhang, et al., "Highly Efficient and Stable ITO-Free Organic Solar Cells Based on Squaraine N-Doped Quaternary Bulk Heterojunction," *Advanced Materials* 36, no. 3 (2024): 2307920.

16. X. Sun, X. Ding, F. Wang, et al., "Binary Organic Solar Cells With >19.6% Efficiency:The Significance of Self-Assembled Monolayer Modification," *ACS Energy Letters* 9 (2024): 4209–4217.

17. Y. J. A. Tamai, "Charge Generation in Organic Solar Cells:Journey Toward 20% Power Conversion Efficiency:Special Issue:Emerging Investigators," *Aggregate* 3, no. 6 (2022): e280.

18. D. Zhang, Y. Ji, Y. Cheng, et al., "High-Efficiency Ultrathin Flexible Organic Solar Cells With a Bilayer Hole Transport Layer," *Journal of Materials Chemistry A* 12, no. 25 (2024): 15099–15105.

19. J. Fu, Q. Yang, P. Huang, et al., "Rational Molecular and Device Design Enables Organic Solar Cells Approaching 20% Efficiency," *Nature Communications* 15, no. 1 (2024): 1830.

20. W. Feng, T. Chen, Y. Li, et al., "Binary All-Polymer Solar Cells With a Perhalogenated-Thiophene-Based Solid Additive Surpass 18 % Efficiency," *Angewandte Chemie International Edition* 136, no. 9 (2024): e202316698.

21. Q. Wan, S. Seo, S. W. Lee, et al., "High-Performance Intrinsically Stretchable Polymer Solar Cell With Record Efficiency and Stretchability Enabled by Thymine-Functionalized Terpolymer," *Journal of the American Chemical Society* 145, no. 22 (2023): 11914–11920.

22. X. Chen, G. Xu, G. Zeng, et al., "Realizing Ultrahigh Mechanical Flexibility and >15% Efficiency of Flexible Organic Solar Cells via a "Welding" Flexible Transparent Electrode," *Advanced Materials* 32, no. 14 (2020): 1908478.

23. W. Xia, B. Zhou, L. Wang, et al., "Insulating Polymer Mediated Stability and Photovoltaic Performance of Organic Solar Cells:Influence of Molecular Weight," *Advanced Functional Materials* 8, no. 48 (2024): 2408340.

24. A. Shafe, H. M. Schrickx, K. Ding, and H. Ade, "Rubber-Toughened Organic Solar Cells:Miscibility-Morphology-Performance Relations," *ACS Energy Letters* 8, no. 9 (2023): 3720–3726.

25. S. Li, M. Gao, K. Zhou, et al., "Achieving Record-High Stretchability and Mechanical Stability in Organic Photovoltaic Blends With a Dilute-Absorber Strategy," *Advanced Materials* 36, no. 8 (2024): 2307278.

26924552, 2025, 2, Downloaded from https://onlinelibrary.wiley.com/doi/10.1002/sus2.70005 by Chalmers Research - Chalmers University Of Technology , Wiley Online Library on [03/06/2026]. See the Terms and Conditions (https://onlinelibrary.wiley.com/terms-and-conditions) on Wiley Online Library for rules of use; OA articles are governed by the applicable Creative Commons License

26. Y. Zheng, S. Zhang, J. B. H. Tok, and Z. Bao, "Molecular Design of Stretchable Polymer Semiconductors:Current Progress and Future Directions," *Journal of the American Chemical Society* 144, no. 11 (2022): 4699–4715.

27. S. Seo, J. W. Lee, D. J. Kim, et al., "Poly (dimethylsiloxane)-Block-PM6 Polymer Donors for High-Performance and Mechanically Robust Polymer Solar Cells," *Advanced Materials* 35, no. 24 (2023): 2300230.

28. Y. Pan, C. Yan, X. Zhao, et al., "11.39% Efficiency $Cu_2ZnSn(S, Se)_4$ Solar Cells From Scrap Brass," *SusMat* 2, no. 2 (2022): 206–211.

29. J.-J. Han, C.-S. Wei, A. Lu, et al., "Visualizing Filler Network to Reveal Structural Mechanisms on Energy Dissipation of Mullins Effect in Silicone Rubber," *Polymer* 301 (2024): 127044.

30. Y. Zhao, X. Zhao, M. Roders, et al., "Melt-Processing of Complementary Semiconducting Polymer Blends for High Performance Organic Transistors," *Advanced Materials* 29, no. 6 (2016): 1605056.

31. S. E. Root, S. Savagatrup, A. D. Printz, D. Rodriquez, and D. J. Lipomi, "Mechanical Properties of Organic Semiconductors for Stretchable, Highly Flexible, and Mechanically Robust Electronics," *Chemical Reviews* 117, no. 9 (2017): 6467–6499.

32. G.-J. N. Wang, Y. Zheng, S. Zhang, et al., "Tuning the Cross-Linker Crystallinity of a Stretchable Polymer Semiconductor," *Chemistry of Materials* 31, no. 17 (2018): 6465–6475.

33. J. W. Lee, T. H. Q. Nguyen, E. S. Oh, et al., "Establishing Co-Continuous Network of Conjugated Polymers and Elastomers for High-Performance Polymer Solar Cells With Extreme Stretchability," *Advanced Energy Materials* 14, no. 26 (2024): 2401191.

34. S. Savagatrup, X. Zhao, E. Chan, J. Mei, and D. J. Lipomi, "Effect of Broken Conjugation on the Stretchability of Semiconducting Polymers," *Macromolecular Rapid Communications* 37, no. 19 (2016): 1623–1628.

35. J. Y. Oh, S. Rondeau-Gagné, Y.-C. Chiu, et al., "Intrinsically Stretchable and Healable Semiconducting Polymer for Organic Transistors," *Nature* 539, no. 7629 (2016): 411–415.

36. M. Q. Zhang, "Dynamic Bonds in Polymers," *Journal of Polymer Science* 62, no. 5 (2024): 785–786.

37. K. Yu, A. Xin, and Q. Wang, "Mechanics of Self-Healing Polymer Networks Crosslinked by Dynamic Bonds," *Journal of the Mechanics and Physics of Solids* 121 (2018): 409–431.

38. N. Y. Kwon, S. H. Park, S. Cho, et al., "Polymer Solar Cells Made With Photocrosslinkable Conjugated Donor-Acceptor Block Copolymers:Improvement in the Thermal Stability and Morphology With a Single-Component Active Layer," *Polymer Chemistry* 13, no. 22 (2022): 3335–3342.

39. Y. He, N. Li, T. Heumüller, et al., "Industrial Viability of Single-Component Organic Solar Cells," *Joule* 6, no. 6 (2022): 1160–1171.

40. E. Dauzon, X. Sallenave, C. Plesse, et al., "Versatile Methods for Improving the Mechanical Properties of Fullerene and Non-Fullerene Bulk Heterojunction Layers to Enable Stretchable Organic Solar Cells," *Journal of Materials Chemistry C* 10, no. 9 (2022): 3375–3386.

41. J. D. Cho, S. Jung, J.-I. Kim, and C. H. Choi, "Improvement of Performance for Flexible Film Dosimeter by Incorporating Additive Agents," *Physics in Medicine and Biology* 69, no. 10 (2024): 105006.

42. J. Han, F. Bao, X. Wang, et al., "Identifying Tunneling Effects of Poly(aryl Ether) Matrices and Boosting the Efficiency, Stability, and Stretchability of Organic Solar Cells," *Cell Reports Physical Science* 2, no. 5 (2021): 100408.

43. J. Xu, S. Wang, G.-J. N. Wang, et al., "Highly Stretchable Polymer Semiconductor Films Through the Nanoconfinement Effect," *Science* 355, no. 6320 (2017): 59–64.

44. J. Wang, C. Han, J. Han, et al., "Synergetic Strategy for Highly Efficient and Super Flexible Thick-Film Organic Solar Cells," *Advanced Energy Materials* 12, no. 31 (2022): 2201614.

45. B. Park, H. Kang, Y. H. Ha, et al., "Direct Observation of Confinement Effects of Semiconducting Polymers in Polymer Blend Electronic Systems," *Advancement of Science* 8, no. 14 (2021): 2100332.

46. I. Angunawela, M. M. Nahid, M. Ghasemi, et al., "The Critical Role of Materials' Interaction in Realizing Organic Field-Effect Transistors via High-Dilution Blending With Insulating Polymers," *ACS Applied Materials & Interfaces* 12, no. 23 (2020): 26239–26249.

47. Q. An, F. Zhang, J. Zhang, et al., "Versatile Ternary Organic Solar Cells: A Critical Review," *Energy & Environmental Science* 9, no. 2 (2016): 281–322.

48. N. Gasparini, A. Salleo, I. McCulloch, and D. Baran, "The Role of the Third Component in Ternary Organic Solar Cells," *Nature Reviews Materials* 4, no. 4 (2019): 229–242.

49. L. Lu, M. A. Kelly, W. You, and L. Yu, "Status and Prospects for Ternary Organic Photovoltaics," *Nature Photonics* 9, no. 8 (2015): 491–500.

50. Z. Peng, K. Xian, Y. Cui, et al., "Thermoplastic Elastomer Tunes Phase Structure and Promotes Stretchability of High-Efficiency Organic Solar Cells," *Advanced Materials* 33, no. 49 (2021): 2106732.

51. D. Sarkar, M. Dhar, A. Das, et al., "Covalent Crosslinking Chemistry for Controlled Modulation of Nanometric Roughness and Surface Free Energy," *Chemical Science* 15, no. 13 (2024): 4938–4951.

52. H. Tan, L. Zhang, X. Ma, L. Sun, D. Yu, and Z. You, "Adaptable Covalently Cross-Linked Fibers," *Nature Communications* 14, no. 1 (2023): 2218.

53. K. Jiang, G. Zhang, G. Yang, et al., "Multiple Cases of Efficient Non-fullerene Ternary Organic Solar Cells Enabled by an Effective Morphology Control Method," *Advanced Energy Materials* 8, no. 9 (2018): 1701370.

54. D. J. Lundberg, C. M. Brown, E. O. Bobylev, et al., "Nested Non-Covalent Interactions Expand the Functions of Supramolecular Polymer Networks," *Nature Communications* 15, no. 1 (2024): 3951.

55. C. Guan, C. Xiao, X. Liu, et al., "Non-Covalent Interactions Between Polyvinyl Chloride and Conjugated Polymers Enable Excellent Mechanical Properties and High Stability in Organic Solar Cells," *Angewandte Chemie International Edition* 135, no. 44 (2023): e202312357.

56. L. A. Galuska, M. U. Ocheje, Z. C. Ahmad, S. Rondeau-Gagné, and X. Gu, "Elucidating the Role of Hydrogen Bonds for Improved Mechanical Properties in a High-Performance Semiconducting Polymer," *Chemistry of Materials* 34, no. 5 (2022): 2259–2267.

57. S. Kamimura, M. Saito, Y. Teshima, et al., "Manipulating the Functionality and Structures of π-Conjugated Polymers Utilizing Intramolecular Noncovalent Interactions Towards Efficient Organic Photovoltaics," *Chemical Science* 15, no. 17 (2024): 6349–6362.

58. Q. Fan, U. A. Méndez-Romero, X. Guo, et al., "Fluorinated Photovoltaic Materials for High-Performance Organic Solar Cells," *Chemistry—An Asian Journal* 14, no. 18 (2019): 3085–3095.

59. G. V. Janjić, S. T. Jelić, N. P. Trišović, D. M. Popović, I. Đorđević, and M. Milčić, "New Theoretical Insight Into Fluorination and Fluorine-Fluorine Interactions as a Driving Force in Crystal Structures," *Crystal Growth & Design* 20, no. 5 (2020): 2943–2951.

60. D. W. Y. Teo, Z. Jamal, Q.-J. Seah, R.-Q. Png, and L.-L. Chua, "General Bis(fluorophenyl Azide) Photo-Crosslinkers for Conjugated and Non-Conjugated Polyelectrolytes," *Journal of Materials Chemistry C* 8, no. 1 (2020): 253–261.

61. K. E. Hung, Y. S. Lin, Y. J. Xue, et al., "Non-Volatile Perfluorophenyl-Based Additive for Enhanced Efficiency and Thermal Stability of Nonfullerene Organic Solar Cells via Supramolecular Fluorinated Interactions," *Advanced Energy Materials* 12, no. 12 (2022): 2103702.

62. Y. Zheng, Z. Yu, S. Zhang, et al., "A Molecular Design Approach Towards Elastic and Multifunctional Polymer Electronics," *Nature Communications* 12, no. 1 (2021): 5701.

63. R.-Q. Png, P.-J. Chia, J.-C. Tang, et al., "High-Performance Polymer Semiconducting Heterostructure Devices by Nitrene-Mediated Pho-

26924552, 2025, 2, Downloaded from https://onlinelibrary.wiley.com/doi/10.1002/sus2.70005 by Chalmers Research - Chalmers University Of Technology , Wiley Online Library on [03/06/2026]. See the Terms and Conditions (https://onlinelibrary.wiley.com/terms-and-conditions) on Wiley Online Library for rules of use; OA articles are governed by the applicable Creative Commons License

tocrosslinking of Alkyl Side Chains," *Nature Materials* 9, no. 2 (2010): 152–158.

64. S. H. Kim, S. Chung, M. Kim, et al., "Designing a Length-Modulated Azide Photocrosslinker to Improve the Stretchability of Semiconducting Polymers," *Advanced Functional Materials* 33, no. 23 (2023): 2212127.

65. J. Kim, G. Zhang, M. Shi, and Z. Suo, "Fracture, Fatigue, and Friction of Polymers in Which Entanglements Greatly Outnumber Cross-Links," *Science* 374, no. 6564 (2021): 212–216.

66. H. Huang, L. Yang, A. Facchetti, and T. J. Marks, "Organic and Polymeric Semiconductors Enhanced by Noncovalent Conformational Locks," *Chemical Reviews* 117, no. 15 (2017): 10291–10318.

67. M. Zhang, L. Zhu, T. Hao, et al., "High-Efficiency Organic Photovoltaics Using Eutectic Acceptor Fibrils to Achieve Current Amplification," *Advanced Materials* 33, no. 18 (2021): 2007177.

68. C. Li, J. Zhou, J. Song, et al., "Non-Fullerene Acceptors With Branched Side Chains and Improved Molecular Packing to Exceed 18% Efficiency in Organic Solar Cells," *Nature Energy* 6, no. 6 (2021): 605–613.

69. J. Y. Chung, A. J. Nolte, and C. M. Stafford, "Surface Wrinkling: A Versatile Platform for Measuring Thin-Film Properties," *Advanced Materials* 23, no. 3 (2011): 349–368.

70. D. E. Martínez-Tong, A. Najar, M. Soccio, et al., "Quantitative Mapping of Mechanical Properties in Polylactic Acid/Natural Rubber/Organoclay Bionanocomposites as Revealed by Nanoindentation With Atomic Force Microscopy," *Composites Science and Technology* 104 (2014): 34–39.

71. D. Rodriquez, J.-H. Kim, S. E. Root, et al., "Comparison of Methods for Determining the Mechanical Properties of Semiconducting Polymer Films for Stretchable Electronics," *ACS Applied Materials & Interfaces* 9, no. 10 (2017): 8855–8862.

72. S. Kim, J.-H. Kim, J.-G. Oh, et al., "Mechanical Behavior of Free-Standing Fuel Cell Electrodes on Water Surface," *ACS Applied Materials & Interfaces* 8, no. 24 (2016): 15391–15398.

73. M. Saito, T. Fukuhara, S. Kamimura, et al., "Impact of Noncovalent Sulfur-Fluorine Interaction Position on Properties, Structures, and Photovoltaic Performance in Naphthobisthiadiazole-Based Semiconducting Polymers," *Advanced Energy Materials* 10, no. 7 (2020): 1903278.

74. M. Schock and S. J. M. Bräse, "Reactive & Efficient:Organic Azides as Cross-Linkers in Material Sciences," *Molecules* 25, no. 4 (2020): 1009.

75. Z. Peng, K. Xian, J. Liu, et al., "Unraveling the Stretch-Induced Microstructural Evolution and Morphology-Stretchability Relationships of High-Performance Ternary Organic Photovoltaic Blends," *Advanced Materials* 35, no. 3 (2023): 2207884.

76. Y. Cai, Q. Li, G. Lu, et al., "Vertically Optimized Phase Separation With Improved Exciton Diffusion Enables Efficient Organic Solar Cells With Thick Active Layers," *Nature Communications* 13, no. 1 (2022): 2369.

77. Z. Lian, Q. Yan, T. Gao, et al., "Perovskite $CH_3NH_3PbI_3$ (Cl) Single Crystals:Rapid Solution Growth, Unparalleled Crystalline Quality, and Low Trap Density Toward 108 cm^{-3}," *Journal of the American Chemical Society* 138, no. 30 (2016): 9409–9412.

78. R. Yu, G. Wu, Y. Cui, et al., "Multi-Functional Solid Additive Induced Favorable Vertical Phase Separation and Ordered Molecular Packing for Highly Efficient Layer-by-Layer Organic Solar Cells," *Small* 17, no. 44 (2021): 2103497.

79. F. Sun, X. Wang, M. Wan, et al., "High Miscibility-Induced Reduction of Trap Density in All-Polymer Solar Cells Using Hybrid Cyclohexyl-Hexyl Side Chains," *Advanced Functional Materials* 33, no. 40 (2023): 2306791.

80. M. Haris, Z. Ullah, S. Lee, et al., "Amplifying High-Performance Organic Solar Cells Through Differencing Interactions of Solid Additive With Donor/Acceptor Materials Processed From Non-Halogenated Solvent," *Advanced Energy Materials* 12, no. 35 (2024): 2401597.

81. Y. Ran, C. Liang, Z. Xu, et al., "Developing Efficient Benzene Additives for 19.43% Efficiency of Organic Solar Cells by Crossbreeding Effect of Fluorination and Bromination," *Advanced Functional Materials* 34, no. 8 (2024): 2311512.

82. X. Wang, J. Wang, P. Wang, et al., "Embedded Host/Guest Alloy Aggregations Enable High-Performance Ternary Organic Photovoltaics," *Advanced Materials* 35, no. 51 (2023): 2305652.

83. Q. Ye, Z. Chen, D. Yang, et al., "Ductile Oligomeric Acceptor-Modified Flexible Organic Solar Cells Show Excellent Mechanical Robustness and Near 18% Efficiency," *Advanced Materials* 35, no. 44 (2023): 2305562.

Supporting Information

Additional supporting information can be found online in the Supporting Information section.

26924552, 2025, 2, Downloaded from https://onlinelibrary.wiley.com/doi/10.1002/sus2.70005 by Chalmers Research - Chalmers University Of Technology , Wiley Online Library on [03/06/2026]. See the Terms and Conditions (https://onlinelibrary.wiley.com/terms-and-conditions) on Wiley Online Library for rules of use; OA articles are governed by the applicable Creative Commons License